PCCP

Accepted Manuscript

This article can be cited before page numbers have been issued, to do this please use: Z. Purohit, D. Verma and B. Tripathi, *Phys. Chem. Chem. Phys.*, 2018, DOI: 10.1039/C8CP02703J.

View Article Online
DOI: 10.1039/C8CP02703J

Electro-analytical investigation of potential induced degradation in mc-silicon solar cells: sodium ions induced inductive loop

Zeel Purohit[a], Deepak Verma[b], Brijesh Tripathi[a],*

[a]*Department of Science, School of Technology, Pandit Deendayal Petroleum University, Gandhinagar – 382007 India.*

[b]*School of Engineering and Applied Science, Ahmedabad University, Ahmedabad – 380009 India.*

*Corresponding Author: Ph. +91 79 2327 5455, Fax. +91 79 2327 5030, E-mail. brijesh.tspv@gmail.com

Abstract

Potential induced degradation of shunt type (PID-s) in multi-crystalline silicon (mc-Si) solar cells is becoming critical for performance reduction of solar panels in large scale photovoltaic (PV) power plants. In this article PID-s has been investigated by applying high voltage stress on mc-Si solar cell for their degradation and recovery and results have been explained on the basis of DC and AC characterization. The efficiency decreases drastically from 15.7% to 2.9% due to the high voltage stress of -800V at 85°C for 48 hours, which is attributed to reduction in shunt resistance and increase in depletion and diffusion capacitances. Reduction in electrical performance due to PID-s has been further explained by morphological, structural and elemental analysis. Observed negative capacitance behaviour in impedance spectra of mc-Si solar cells after PID-s has been attributed to structural deformation caused by potential induced migration of sodium ion (Na^+) into mc-Si. The structural deformation induced by potential induced migration of Na^+ ion has been confirmed by using non-destructive and lattice strain sensitive micro-Raman spectroscopy. The obtained

View Article Online
DOI: 10.1039/C8CP02703J

experimental results have been correlated with existing theoretical understanding of p-n junction solar cells to explain consequences of the PID-s.

Keywords: reliability, crystalline silicon solar cells, potential-induced degradation (PID), impedance spectroscopy (IS).

1 Introduction

In megawatt-scale solar photovoltaic (PV) power plants, multi-crystalline silicon (mc-Si) solar modules are connected in series and parallel combination in order to enhance the voltage and current outputs of an array respectively. The solar cells inside the encapsulated PV modules experience significant voltage stress with respect to the aluminium frame. This high voltage stress is responsible for adverse effects on the power output of solar PV module, which is known as potential-induced degradation (PID) [1-5]. In recent times, PID has been given more attention as the major reliability issue due to frequent mid-life failures of modules in larger scale power plants [5]. For the developing countries like India, with an aggressive target of 100 GW by 2022 [6], it becomes important to consider reliability issues associated to mid-life failures. The PID-s affected modules have an enormously declined power output over a period of time under harsh environmental conditions [7]. Several studies have been done towards the identification and investigation of PID-s affected modules under various climatic and potential conditions [8-11]. Further, solar PV modules subjected to PID-s are also influenced by the properties of anti-reflection coatings (ARCs) [12, 13], encapsulating materials [14-17], covering glass [18, 19] and system topologies [12, 13, 20, 21].

In recent years, various PID experiments have been performed on different types of solar cell technologies and also, many efforts have been made in order to evaluate the origin of the PID-s phenomena [22-25]. The migration of sodium ions (Na^+) under strong electric

View Article Online
DOI: 10.1039/C8CP02703J

field has been considered as a major factor causing PID [23]. Moreover, the PID of mono-crystalline silicon solar cells has been studied with respect to the different orientations of crystal planes [26]. In addition, atomic modelling using first principle density functional theory (DFT) calculations for Na accumulation has been performed to envisage the effect of Na impurities on the electronic structure of silicon material [27, 28]. The reduction in the electrical output parameters under the influence of PID-s in relation to the micro-structural defects in the material through electro-analytical method has not been well explored.

Impedance spectroscopy (IS) is an alternating current (AC) characterization technique, which is widely used for characterization of solid-state electrolytic device such as solar cell [29-32]. This technique helps to investigate the dynamic behaviour of electro-analytical parameters of solar cell under small amplitude sinusoidal perturbating AC signal superimposed on a suitable direct current (DC) voltage. The response of the solar cell can be used to calculate the overall impedance (Z, a complex number) as a function of frequency (f). Various electronic processes in the solar cell occur on different time scales, which result in semicircles of different sizes in the complex plane referred as Nyquist plot (Z'-Z"). Nyquist plot consists of a number of semicircles depending on physical processes happening at various interfaces in the solar cell [30]. Each semicircle represents particular physical process described in terms of series or parallel combination of Voigt elements (a combination of a resistor (R) and capacitor (C) or an inductor (L)). IS has been widely used to investigate electronic processes in the solar cell such as surface transport, diffusion and recombination associated to the bulk and the interface [29-36]. Moreover, IS has been also used to study PID phenomenon by Opera et al. [35], however in-depth analysis and explanation has yet to be thoroughly discussed.

This article explains the electrical performance output of mc-Si solar cells subjected to PID-s with a better understanding of the physical processes behind the reduction in open-

View Article Online
DOI: 10.1039/C8CP02703J

circuit voltage (V_{OC}) and maximum output power (P_{max}). The experimental DC current density-voltage (J-V) characteristics before and after PID-s have been theoretically fitted using two-diode model and a drastic reduction in the electrical output of solar cells has been further explained using IS. This article reports various physical processes associated to the p-n junction deterioration caused by migrated Na^+ impurity concentration. In addition, an increased recombination through micro-structurally deformed grain boundaries due to Na^+ movement has been found responsible for the reduction in the efficiency (η) of commercially available mc-Si solar cell.

2 Experimental details

Encapsulated commercially available mc-Si solar cells of 1 cm^2 area were used for study, marked as 'CS-1', 'CS-2' and 'CS-3'. The mc-Si cells (n^+-p-p^+), typically contain aluminium (Al) back surface field (BSF) structure with a phosphorus-doped n^+ emitter, a boron-doped p-type base, and an Al-doped p^+ BSF, with Ag and Al metalized contacts at the front (emitter) and back (base) surfaces, respectively with SiN_x ARC layer on top. The 'CS-1' represents the fresh solar cell, 'CS-2' represents degraded solar cell after subjecting 'CS-1' to an applied voltage of 800V for 48 hours in a configuration as shown in Fig. 1. 'CS-3' represents the recovered solar cell by applying reverse polarity voltage of 800 V for 240 hours to the 'CS-2'. The solar cells were embedded in sandwich structure of tempered cover glass as the front window material; ethylene vinyl acetate (EVA) as front and back encapsulation material and polyvinyl fluoride (PVF) is used as the encapsulating back sheets. The PID tests were carried out by applying a high voltage stress of 800 V (at a temperature of 85 °C and relative humidity of 65 %RH) across the encapsulated solar cell by connecting the positive electrode to the aluminium foil placed on the front cover glass and negative electrode to the shorted terminals (Fig. 1). To evaluate the J-V characteristics, CS-1', 'CS-2', and 'CS-

View Article Online
DOI: 10.1039/C8CP02703J

3' were measured under standard test conditions (25°C, 1000 Wm^{-2}, AM1.5G spectrum) using solar simulator (SS80AAA, Photoemission Tech., USA) equipped with AM1.5G filter and source measuring unit (U2722A, Agilent). The surface morphological and elemental analyses were carried out using field emission scanning electron microscope (FESEM, Carl Zeiss, Ultra-55, 1-20 kV) equipped with energy dispersive X-ray spectrometry (EDX, Oxford Instruments). IS and capacitance-voltage (C-V) measurements were carried out under dark conditions using a three electrode potentiostat (660D, CH Instruments) equipped with a frequency response analyser with 5 mV AC perturbation signal in the frequency range of 0.1 Hz to1 MHz. Micro-Raman measurements were carried out using (Renishaw inVia system) with an excitation laser beam of 532 nm.

3 Theoretical details

3.1 Theory of DC equivalent circuit

The two-diode based equivalent circuit of the solar cells is shown in Fig. 2. The reverse saturation current densities of the first and second diodes are denoted as J_{01} and J_{02} and ideality factors of the first and second diode are represented as n and m, respectively. The parallel/shunt resistance (R_{sh}), and series resistance (R_S) are included to quantify the deviation of the current density-voltage (J-V) characteristics from the ideal behaviour. The two-diode model equation for illuminated solar cell can be expressed as [33]:

$$J = J_{PH} - J_{01}\left(exp\frac{q(V_j+JR_s)}{nk_BT} - 1\right) - J_{02}\left(exp\frac{q(V_j+JR_s)}{mk_BT} - 1\right) - \frac{V_j+JR_s}{R_{sh}} \quad (1)$$

where, V_j represents bias voltage, J_{PH} represents light generated current density, q represents the charge of an electron, k_B represents the Boltzmann constant, and T represents the absolute temperature. The two-diode model is used to fit experimental data using the MATLAB/Simulink code to estimate R_S, R_{sh}, n and m of the solar cell subjected to PID-s. The performance parameters of the silicon solar cell namely, short-circuit current density

View Article Online
DOI: 10.1039/C8CP02703J

(J_{SC}), V_{OC}, the fill factor (FF) represent the extent of pseudo rectangular shape for the non-linear J-V curve, are related to η as per following expression:

$$\eta = \frac{V_{OC} \times J_{SC} \times FF}{(A \times P_{in})} \quad (2)$$

Here, P_{in} represents the power input through the incident light radiation per unit area and A represents the area of solar cell.

3.2 Theory of AC equivalent circuits

Electro-analytical IS technique has been extensively used as the powerful probing characterization to manifest the physical fundamental processes in the devices, (e.g. crystalline silicon solar cell) with linear sweep voltammetry [31, 32]. Furthermore, it serves the understanding associated to charge carrier transport kinetics, which is mainly governed by minority carrier diffusion and recombination. The p-n junction space charge layer of mc-Si solar cell is mainly governed by two circuit elements: junction resistance (R_j) and junction capacitance (C_j). The effective junction resistance (R_j) is approximately equal to the sum of, R_{sh} and diffusion resistance (R_d). The R_d can be extracted from the voltage dependence of current density under intermediate and strong forward bias and governed by diode ideality factor and reverse saturation current as given by following expression [33]:

$$R_d = \frac{mk_BT}{q \cdot exp\left(\frac{qV_j}{mk_BT}\right)} \left[\frac{1}{J_{0e}} + \frac{1}{J_{0b}}\right] \quad (3)$$

where, V_j represents the junction voltage, J_{0e} and J_{0b} represent the current density of the emitter and the base, respectively. The effective junction capacitance (C_j) is approximately equal to the sum of capacitance of depletion layer(C_{dl}),which is also known as transition capacitance (C_T) and diffusion capacitance (C_μ).For the case of depletion layer width much greater than Debye length, which is the case under reverse and low forward bias,C_{dl}^{-2} varies linearly with respect to bias as given by following equation [32]:

View Article Online
DOI: 10.1039/C8CP02703J

$$C_j = \frac{\varepsilon_r \varepsilon_0}{w_0 V_j^{1/2}} \quad (4)$$

where, w_0 represents depletion width, $w = w_0 V_{sc}^{1/2}$, ε_r and ε_0 represent the relative and absolute permittivity respectively. The w_0 is equal to $\left(2\varepsilon_r\varepsilon_0/qN\right)^{1/2}$ where, N represents the charge concentration. At intermediate and strong forward bias the capacitance associated with the homogenous layer thickness L (thickness of solar cell) is known as diffusion capacitance or chemical capacitance (C_{LH}), which depends on the minority carrier concentration and effective density of states in the conduction band, as expressed by following equation [29, 30, 32]:

$$C_{LH} = \frac{q^2 L n_0}{k_B T} \exp\left(\frac{qV_j}{k_B T}\right) \quad (5)$$

The sign of V_j is positive or negative, depending on whether the diode junction is forward ($+V_{FB}$) or reverse ($-V_{RB}$) biased. Holes from the p^+ side of the low-high (LH) interface (p-p^+ BSF) diffuse into the p side to form a hole-accumulation layer. The electric field of p-p^+ prevents diffusing electrons from the n^+-p junction back into p layer. The physical terms of AC circuit elements (used in Eq. (6)) for fresh solar cell can be described as: R_s represents series resistance to photo-generated charge carriers while they flow out of the solar cells to the external contacts, R_j represents junction resistance, R_{LH} represents p-p^+ diffusion resistance, C_j represents the junction capacitance, C_{LH} represents the p-p^+ capacitance offered by the high low. If the electrode is non-polarizable, then the system can be modelled by introducing a resistance R_j parallel to the capacitance C_j, which is known as simplified Randle's circuit [34]. Eventually, the circuit consists of a series connection of a material resistance R_s with a parallel combination of a charge transfer resistance R_j and a double layer capacitance C_j (Fig. 3(a)). The impedance of the system can be written as:

$$Z(\omega) = R_s + \frac{R_j}{1+\omega^2 R_j^2 C_j^2} - j\frac{\omega R_j^2 C_j}{1+\omega^2 R_j^2 C_j^2} + \frac{R_{LH}}{1+\omega^2 R_{LH}^2 C_{LH}^2} - j\frac{\omega R_{LH}^2 C_{LH}}{1+\omega^2 R_{LH}^2 C_{LH}^2} \quad (6)$$

View Article Online
DOI: 10.1039/C8CP02703J

The impedance spectra of CS-2 and CS-3 solar cells can be explained by Eq. (7). Further, the inductive part can be understood in terms of negative capacitance described recently in reference [36] and shown in Fig. 3(b). As described earlier, a negative capacitance represents the inductive behaviour of a device with the frequency which is expected to have capacitive response [37]:

$$Z(\omega) = R_s + \frac{R_j}{1+\omega^2 R_j^2 C_j^2} - j\left(L\omega + \frac{\omega R_j^2 C_j}{1+\omega^2 R_j^2 C_j^2}\right) + \frac{R_{LH}}{1+\omega^2 R_{LH}^2 C_{LH}^2} - j\left(L\omega + \frac{\omega R_{LH}^2 C_{LH}}{1+\omega^2 R_{LH}^2 C_{LH}^2}\right) \quad (7)$$

4. Results and discussion

4.1 DC analysis of PID-s affected solar cell

Figure 4(a) shows the J-V characteristics of mc-Si solar cells for the cases CS-1, CS-2 and CS-3 and corresponding data has been listed in Table 1. A drastic reduction in J-V performance has been observed for CS-2 as compared to CS-1 due to PID-s, where η decreases from 15.7% to 2.9% after 48 hours of PID-s. The value of η depends on the I_{sc}, V_{oc} and FF, although J_{SC} has not been affected much by PID-s as compared to V_{OC}. The V_{OC} decreases significantly from 0.59 V to 0.25 V, which is governed by the value of R_{sh} in Eq. (1). Under PID-s, R_{sh} has decreased from 3000 Ω to 8.7 Ω indicating a higher level of leakage path across the junction restricting minority charge carrier accumulation in QNR, which explains drastic reduction in V_{OC} under PID-s. Moreover, ideality factors n and m have been obtained from two-diode model (Eq. (1)) for CS-1 as 1.5 and 2.2 respectively. For CS-2 the values of n and m increased to 2.5 and 3.5, which indicate the increase in recombination in SCR and QNR regions and degradation in p-n junction. The explanation of increase in ideality factor is in accordance with Lausch et al. [38]. In the recovered solar cell (CS-3), the V_{OC} and R_{sh} have increased from 0.25 V to 0.43 V and from 8.7 Ω to 17 Ω respectively, which can be explained by decrease in leakage path across p-n junction during recovery. Decrease in reverse saturation current density from 9.42×10^{-5} mAcm^{-2} to 1.57×10^{-5} mAcm^{-2}

View Article Online
DOI: 10.1039/C8CP02703J

further supports the decrease in leakage path. The V_{OC} is related to reverse saturation current density by, $V_{OC} \approx (k_B T/q)\ln(J_{PH}/J_0)$ [39], which indicates that V_{OC} would increase with decrease in J_0. Figure 4(b) illustrates the junction resistance, R_j with respect to bias voltage. The decrease in shunt resistance, R_{sh} by two order of magnitudes has been observed for CS-2 and CS-3 as compared to CS-1. The recombination flux governs the R_j beyond the knee voltage (≈ 0.4 V) as per following expression: $R_j = (dJ_{rec}/dV_j)^{-1}$, where J_{rec} represents recombination current density [29, 33]. The main reason behind higher recombination in CS-2 is the increase in leakage path due to defects, whereas in CS-3 the recombination is lower as compared to CS-2 due to improvement in junction quality due to partial recovery. The nature and distribution of positive ions has been explored in detail through elemental analysis of degraded solar cells.

4.2 Correlation of morphological and elemental analysis with electrical characterization

To investigate the effect of PID-s on the surface morphology of mc-Si solar cells at the micro-scale, the PID-s affected solar cells have been characterized by using FESEM. Figure 5 shows the surface morphology and the EDX analysis of mc-Si solar cells after PID-s. It is observed from FESEM image that there are micro-structural defects on the surface of PID-s affected solar cell due to high voltage stress. Moreover, EDX analysis of degraded solar cell reveals that there is a significant amount of sodium impurities with 10 at.% of elemental composition (the marked defected region of Fig. 5). The defected region has been further investigated by the EDX mapping of Si, Na, O, N elements as shown in Fig. 5. There are three dark spots in Si mapped image, which signifies the absence of Si atoms in that region. By mapping sodium element it is revealed that there is high concentration of sodium atoms at the dark spots. The elemental mapping of O and N shows their uniform presence within the allowed limits. This sodium impurity plays a key role towards the

View Article Online
DOI: 10.1039/C8CP02703J

progression of PID-s [23-25]. The micro-structural defects are responsible to initiate the stacking faults through grain boundaries and allow Na^+ to drift through SiN_x layer and finally get a path to penetrate into n^+-p junction. After entering into n^+-emitter layer, the Na^+ ions are neutralized by free electrons and their further motion in the stacking fault is governed by diffusion process rather than drift process [40]. In order to explore the effect of sodium impurity on the electrical performance of solar cell, electro-analytical investigation has been carried out using AC IS as detailed in next section.

4.3 AC impedance analysis of PID-s affected solar cell

Figure 6 shows the impedance measurement results of CS-1, CS-2 and CS-3. Figure 6(a) demonstrates the Nyquist plots of CS-1 in the bias range from -1 V to + 0.3 V. The dotted curve represents the experimental data, which has been fitted with the theoretical AC equivalent circuit governed by Eq. (6) as shown by solid curve. The diameter of impedance spectra (nearly semicircle) increases with the reverse bias due to increase in the width of depletion region, which offers high impedance, whereas, under forward bias, impedance is decreasing due to decrease in the width of depletion region. The R_j increases from 2795 Ω to 3607 Ω while increasing reverse bias from 0 V to -1 V and decreases to 350 Ω with forward bias value of 0.3 V. The junction capacitance, C_j of CS-1 varies from 9.79 μF to 1.2 μF for +0.3 V to -1 V. Figure 6(b) shows the AC impedance spectra of PID-s affected solar cell, i.e. CS-2. The R_j increases from 6.15 Ω to 15 Ω while increasing reverse bias and decreases to 2.32 Ω with a value of forward bias equal to +0.3 V. The junction capacitance offered by CS-2 varies from 10.9 μF to 0.16 μF for an applied bias of +0.3 V to -1 V. The R_j has decreased for CS-2 as compared to CS-1 due to presence of Na^+ ions creating shunt path across the n^+-p junction at the deformed regions as confirmed by elemental analysis of defected area shown in Fig. 5. Similar observation has been obtained from DC analysis

View Article Online
DOI: 10.1039/C8CP02703J

indicating the increased leakage current across the n^+-p junction. Further, the negative capacitance has been observed at higher frequency for bias voltage in the range from 0 V to +0.3 V, which has been attributed to inductive behaviour of n^+-p junction originated after PID-s. In general, inductive behaviour occurs when excess charge carriers are injected in a small nanoscale dimension into the material, which gives rise to a negative capacitance. Considering the present work, there are two possible interpretations of negative capacitance for Na^+ contaminated stacking faults under PID-s: (1) The Na^+ impurity injection through stacking faults modulates the bulk conductivity of solar cells, which may yield the inductive nature [41, 42], (2) The presence of excessive Na^+ impurities delocalize the minority charge accumulation process and further leads to an abrupt change in junction capacitance values. This charge delocalization effect may give rise to the occurrence of inductive behaviour [43, 44]. The negative capacitance indicates the presence of parasitic inductance and the overall contribution is taken care by a series inductor L as shown in Fig. 6(b). The value of L increases from 0.062 μH to 0.116 μH for CS-2 for applied bias from -1 to +0.3 V. The negative capacitance is attributed to the presence of Na^+ ions across the p-n junction, which creates defects and trap states leading to charge delocalization [36, 45]. Under forward bias condition, electrons fill-up the empty trap states at the interface. Consequently overall charge at interface decreases with increasing bias leading to negative equivalent capacitance. Figure 6(c) demonstrates the Nyquist curve for CS-3, the R_j increases from 7.9 Ω to 31.4 Ω for the range of applied bias from +0.3 V to -1 V. The inductance values remain in the range from 0.28 μH to 0.46 μH for CS-3, which is high as compared to CS-2. The possible reason behind the increment in R_j as compared to CS-2 is the decrease in leakage path due to reverse migration of Na^+ ions across the junction, but some significant structural deformation has still been contributing towards the irreversible charge dislocation process, which is represented by high value of L in CS-3. Figure 6(d) shows the frequency dependent impedance of CS-1, CS-

View Article Online
DOI: 10.1039/C8CP02703J

2 and CS-3 for comparison purpose. The change in R_j and C_j is clearly evident from the values of impedance and slope of the curves for CS-1, CS-2 and CS-3 respectively.

Figure 7 shows variation in the time constant with respect to applied bias. The time constant represents the effective life time of charge carriers in the solar cell and has been extracted from the product of R_j and C_j values at maxima of Nyquist plot shown in Fig. 6(a-c). The minority carrier lifetime has been calculated at the voltage of 0.3 V for CS-2 and CS-3 as 0.73 μs and 0.89 μs, which is lower as compared to 4.15 ms for CS-1, thus indicating a higher recombination under the influence of defects created by Na^+ ions.

4.4 C-V analysis of PID-s affected solar cell

Figure 8 shows the Mott-Schottky plot for CS-1 (CS-2 and CS-3 in the insert), governed by following expression: $C_j^{-2} \approx 2\left(V_{bi} - V_j\right)/q\varepsilon N_A$ [46], where V_{bi} represents the built-in potential, N_A represents the base doping concentration and ε represents product of the permittivity of free space and dielectric constant of silicon. The Mott-Schottky curve slope and intercept represents the build-in potential and base doping concentration. The slope $\left(2/q\varepsilon N_A\right)$ and intercept $\left(2V_{bi}/q\varepsilon N_A\right)$ of the fitted lines gives a value of V_{bi} and N_A respectively for CS-1, which has been obtained as 0.61 V and 1.13×10^{16} cm^{-3}. Similarly, the V_{bi} and N_A for CS-2 and CS-3 are obtained as 0.26 V, 1.74×10^{17} cm^{-3} and 0.45 V, 1.20×10^{17} cm^{-3} respectively. The increase in N_A for CS-2 as compared to CS-1 has been attributed to migration of Na^+ ions into the base material. The effect of partial recovery is clearly seen through the reduction of N_A for CS-3 as compare to CS-2, which indicates out diffusion of Na^+ ions during recovery process. The out diffusion also improved V_{bi} as reflected from increase in V_{OC} from 0.25 V to 0.43 V.

View Article Online
DOI: 10.1039/C8CP02703J

4.5 Raman analysis

Raman spectrometry has been proven as the highly efficient characterization technique to probe the lattice defects [47-49], doping concentration [50, 51] and impurities evaluation corresponding to lattice vibrational modes in the materials. The shift and broadening of phonon peaks indicate the lattice strain induced by defects [49]. To investigate Na^+ induced lattice disorder in mc-Si solar cell, the micro-Raman signals have been analysed. Figure 9 depicts the Raman spectra obtained for Initial and PID-s affected cells (taken at different PID-s affected regions named as the PID-1, PID-2 and PID-3 as schematically shown by 1, 2 and 3 in the insert of Fig. 9). A significant variation has been observed for all characteristic peaks over the wide range of wavenumbers from 100 cm^{-1} to 1500 cm^{-1} for PID-s affected solar cell as compared to Initial. First order transverse optical phonon peak (1TO) located at 520 cm^{-1} has been obtained for initial mc-Si solar cells, whereas for PID-s affected solar cells intensity of 1TO strongly decreases and slightly shifts towards higher frequency. The decreasing intensity and shift is mainly attributed to Na^+ induced localized defects in PID-s affected solar cells, which is more evident for PID-3 (most defected/dark region) as compared to initial. This observation has a strong correlation with EDX analysis (see Fig. 5) which is showing a higher concentration of Na^+ defects for PID-3 and correspondingly reflects the decrease in order of crystallinity of Si material [47]. In addition, optical phonons are strongly affected by the presence of Na^+ impurities due to their small coherence length which gives information about local environment. Whereas, large coherence length of acoustic phonons gives an ease to investigate deeply buried lattice delocalization caused by Na^+ induced defects. The broad peaks at 302 and 940 cm^{-1} correspond to the second order transverse acoustic phonon mode (2TA) and transverse optical phonon mode (2TO) for the initial and PID-s affected regions. Similar observations have been found for second order overtone peaks with decrease in intensity at the PID-s affected regions (302 and

View Article Online
DOI: 10.1039/C8CP02703J

940 cm^{-1} in Fig. 8). Moreover, at higher frequency other characteristic peaks have been observed for highly affected region, PID-3. These peaks are mostly influenced by higher concentration of Na^+ impurities located at deformed region that causes a significant deterioration in local crystallinity of solar cell due to PID-s.

5. Conclusions

In this article, PID-s has been investigated by applying high voltage stress on mc-Si solar cell and results have been explained using electrochemical analysis by DC and AC characterization. Reduction in electrical performance due to PID-s has been explained by morphological, structural and elemental analysis. Furthermore, observed negative capacitance behaviour in impedance spectra of mc-Si solar cells after PID-s has been attributed to structural deformation caused by potential induced migration of Na^+ into mc-Si. The Na^+ ion migration has been analysed using non-destructive and lattice strain sensitive micro-Raman spectroscopy. The decrease in efficiency from 15.7% to 2.9% due to the applied voltage of -800V at 85°C for 48 hours has been explained through the reduction in shunt resistance, increase in depletion and diffusion capacitances and lattice disorder.

Conflicts of interest

There are no conflicts of interest to declare.

Acknowledgements

The authors acknowledge Solar Research and Development Centre (SRDC), PDPU for providing the facilities and support.

References

View Article Online
DOI: 10.1039/C8CP02703J

1. G. Mon, L. Wen, R. Ross and D. Adent, Proceedings of the 18th IEEE Photovoltaic Specialists Conference, Las Vegas, NV, USA, 1985, pp. 1179–1185.

2. S. Pingel, O. Frank, M. Winkler, S. Daryan, T. Geipel, H. Hoehne and J. Berghold, Proceedings of the 35th IEEE Photovoltaic Specialists Conference, Honolulu, HI, USA,2010, pp. 2817–2822.

3. S. Pingel, O. Frank, M. Winkler, S. Daryan, T. Geipel, H. Hoehne and J. Berghold, Proceedings of the 35th IEEE Photovoltaic Specialists Conference, Honolulu, HI, USA, 2010, pp. 2817–2822.

4. P. Hacke, K. Terwilliger, S. Glick, D. Trudell, N. Bosco, S. Johnston and S. Kurtz, Proceedings of the 35th IEEE Photovoltaic Specialists Conference, Honolulu, HI, USA,2010, pp. 000244–000250.

5. M. Köntges, S. Kurtz, C.E. Packard, U. Jahn, K. Berger, K. Kato, T. Friesen, H. Lui and M.V. Iseghem, Review of Failures of Photovoltaic Modules, Performance and Reliability of Photovoltaic Systems, External final report IEA-PVPS, March 2014.

6. Government announces Trajectory to achieve its targets of commissioning 100 GW of Solar generating capacity and 60 GW of Wind power by 2022. http://pib.nic.in/newsite/PrintRelease.aspx?relid=173830 (accessed on 22-06-2018).

7. J. Berghold, S. Koch, S. Pingel, S. Janke, A. Ukar, P. Grunow and T. Shioda, Proceedings of SPIE, San Diego, CA, USA, 2015, vol. 9563, pp. 95630A.

8. P. Hacke, R. Smith, K. Terwilliger, G. Perrin, B. Sekulic and S. Kurtz, Prog. Photovoltaics, 2014, 22, 775–783.

9. P. Hacke, K. Terwilliger, R. Smith, S. Glick, J. Pankow, M. Kempe, S. K. I. Bennett and M. Kloos, Proceedings of the 37th IEEE Photovoltaic Specialists Conference, Seattle, WA, USA, 2011, pp. 000814–000820.

View Article Online
DOI: 10.1039/C8CP02703J

10. M. Schütze, M. Junghänel, M. Koentopp, S. Cwikla,S. Friedrich, J. Müller and P. Wawer, Proceedings of the 37th IEEE Photovoltaic Specialists Conference, Seattle, WA, USA, 2011, pp. 000821–000826.

11. N. G. Dhere, N. S. Shiradkar and E. Schneller, IEEE Journal of Photovoltaics, 2014, 4, 654–658.

12. J. Berghold, O. Frank, H. Hoehne, S. Pingel, B. Richardson and M. Winkler, Proceedings of the 25th European Photovoltaic Solar Energy Conference and Exhibition, Valencia, Spain, 2010, pp. 3753–3759.

13 S. Pingel, O. Frank, M. Winkler, S. Daryan, T. Geipel, H. Hoehne and J. Berghold, Proceedings of the 35th IEEE Photovoltaic Specialists Conference, Honolulu, HI, USA, 2010, pp. 2817–2822.

14. J. Berghold, S. Koch, B. Frohmann, P. Hacke and P. Grunow, Proceedings of the 40th IEEE Photovoltaic Specialists Conference, Denver, CO, USA, 2014, pp. 1987–1992.

15. S. Yamaguchi, A. Masuda and K. Ohdaira, Sol. Energy Mater. Sol. Cells, 2016, 151, 113–119.

16. M. López-Escalante, L.J. Caballero, F. Martín, M. Gabás, A. Cuevas and J. Ramos-Barrado, Sol. Energy Mater. Sol. Cells, 2016, 144, 691–699.

17. J. Kapur, A. Bennett, J. Norwood, B. Hamzavytehrany and I. Kueppenbender, Proceedings of the 28th European Photovoltaic Solar Energy Conference and Exhibition, Paris, France, 2013, pp. 476–479.

18. M. Kambe, K. Hara, K. Mitarai, S. Takeda, M. Fukawa, N. Ishimaru and M. Kondo, Proceedings of 42nd IEEE Photovoltaic Specialist Conference, Tampa, FL, USA, 2013, pp. 3500–3503.

19. J. Oh, S. Bowden and G. TamizhMani, IEEE Journal of Photovoltaics, 2015, 5, 1540–1548.

View Article Online
DOI: 10.1039/C8CP02703J

20. M.B. Koentopp, M. Krober and C. Taubitz, IEEE Journal of Photovoltaics, 2016, 6, 252–257.

21. S. Pingel, S. Janke and O. Frank, Proceedings of the 27th European Photovoltaic Solar Energy Conference and Exhibition, Frankfurt, Germany, 2012, pp. 3379–3383.

22. P. Hacke, K. Terwilliger, R. Smith, S. Glick, J. Pankow, M. Kempe, S.K.I. Bennett and M. Kloos, Proceedings of the 37th IEEE Photovoltaic Specialists Conference, Seattle, WA, USA, 2011, pp. 000814–000820.

23. V. Naumann, D. Lausch, S. Großer, M. Werner, S. Swatek, C. Hagendorf and J. Bagdahn, Energy Procedia, 2013, 33, 76–83.

24. V. Naumann, D. Lausch, A. Graff, M. Werner, S. Swatek, J. Bauer, A. Hähnel, O. Breitenstein, S. Großer and J. Bagdahn, Phys. Status Solidi RRL, 2013, 7, 315–318.

25. P. Hacke, R. Smith, K. Terwilliger, S. Glick, D. Jordan, S. Johnston, M. Kempe and S. Kurtz, Proceedings of the 38thIEEE Photovoltaic Specialists Conference, Austin, TX, USA, 2012, pp. 1–8.

26. S. Yamaguchi, A. Masuda and K. Ohdaira, Jpn. J. Appl. Phys., 2016, 55, 04ES14.

27. B. Ziebarth, M. Mrovec, C. Elsässer and P. Gumbsch, J. Appl. Phys., 2014, 116, 093510.

28. J. Parka, M. Chan, J. Appl. Phys., 2018, 123, 161560.

29. J.E. Garland, D.J. Crain, J.P. Zheng, C.M. Sulyma and D. Roy, Energy Environ. Sci., 2011, 4, 485–498.

30. J.E. Garland, D.J. Crain and D. Roy, Sol. Energy, 2011, 85, 2912–2923.

31. R.A. Kumar, M.S. Suresh and J. Nagaraju, IEEE Trans. Power Electron., 2006, 21, 543–548.

32. I. Mora-Sero, G. Garcia-Belmonte, P.P. Boix, M.A. Vazquez and J. Bisquert, Energy Environ. Sci., 2009, 2, 678–686.

View Article Online
DOI: 10.1039/C8CP02703J

419 33. P. Yadav, B. Tripathi, K. Pandey and M. Kumar, Phys. Chem. Chem. Phys., 2014, 16,
420 15469.
421 34. D.J. Crain, S. E. Rock, J. E. Garland and D. Roy, Curr. Appl. Phys., 2013, 13, 2087–
422 2097.
423 35. M.I. Oprea, Proceeding of the 43rd IEEE Photovoltaic Specialists Conference (PVSC),
424 Portland, OR, 2016, pp. 1575-1579.
425 36. J. Panigrahi, Vandana, R. Singh, N. Batra, J. Gope, M. Sharma, P. Pathi, S.K. Srivastava,
426 C.M.S. Rauthan and P.K. Singh, Sol. Energy, 2016, 136, 412–420.
427 37. M. Ershov, H.C. Liu, L. Li, M. Buchanan, Z.R. Wasilewski and A.K. Jonscher, IEEE
428 Trans. Electron Devices 1998, 45, 2196–2206.
429 38. D. Lausch, V. Naumann, O. Breitenstein, J. Bauer, A. Graff, J. Bagdahn and C.
430 Hagendorf, IEEE Journal of Photovoltaics, 2014, 4, 834–840.
431 39. C.S. Solanki, Solar Photovoltaics: Fundamental, technologies and applications, Prentice
432 Hall, India, 2nd ed., 2011.
433 40. W. Luo, Y. Khoo, P. Hacke, V. Naumann, D. Lausch, S. P. Harvey, J. P. Singh, J. Chai,
434 Y. Wang, A. G. Aberle and S. Ramakrishna, Energy Environ. Sci., 2017, 10, 43-68.
435 41. J.J.H. Van den Biesen, Solid-St. Electron., 1990, 33, 1471-1476.
436 42. M.A. Green and M.W. Gunn, Phys. Status Solidi (a), 1973, 19, K93.
437 43. I. Mora-Sero, J. Bisquert, F. Santiago and G. Belmonte., Nano Lett., 2006, 6, 640-650.
438 44. A. Zohar, N. Kedem, I. Levine, D. Zohar, A. Vilan, D. Ehre, G. Hodes and D. Cahen,
439 Phys. Chem. Lett. 2016, 7, 191−197.
440 45. X. Wu, E.S. Yang, and H.L. Evans, J. Appl. Phys., 1990, 68, 2845.
441 46. A. Goetzberger, J. Knobloch and B. Voss, Crystalline silicon solar cells, J. Wiley, New
442 York, 1998.

View Article Online
DOI: 10.1039/C8CP02703J

443 47. C. Villeneuve, V. Paillard, K.K. Bourdelle, I. Cayrefourcq, A. Boussagol and M.
444 Kennard, Nuclear Instruments and Methods in Physics Research Section B: Beam
445 Interactions with Materials and Atoms, 2006, 253, 182-186.
446 48. N. M. Johnson, F. A. Ponce, R. A. Street and R. J. Nemanich, Phys. Rev. B,1987, 35,
447 4166.
448 49. G. Popovici, G. Y. Xu, A. Botchkarev, W. Kim, H. Tang, A. Salvador and H. Morkoç, R.
449 Strange and J. O. White, J. Appl. Phys., 1997, 82, 4020.
450 50. H. Q. Ni, Y. F. Lu, Z. Y. Liu, H. Qiu, W. J. Wang, Z. M. Ren, S. K. Chow and Y. X. Jie,
451 Appl. Phys. Lett., 2001, 79, 812.
452 51. M. Becker, U. Gösele, A. Hofmann and S. Christiansen, J. Appl. Phys., 2009, 106,
453 074515.
454
455
456
457
458
459
460
461
462
463
464
465
466
467

View Article Online
DOI: 10.1039/C8CP02703J

468 **Table 1:** Performance parameters of solar cells extracted from DC characterization

Parameters	**J_{SC} (mA)**	**V_{OC} (V)**	**J_{01} (mA cm^{-2})**	**J_{02} (mA cm^{-2})**	**R_s (Ω)**	**R_{sh} (Ω)**	**n**	**m**	**FF (%)**	**η (%)**
CS-1	38.06	0.59	8.48 $\times10^{-9}$	3.88 $\times10^{-6}$	0.8	3000	1.5	2.2	70	15.7
CS-2	38.31	0.26	9.42 $\times10^{-5}$	5.33 $\times10^{-4}$	1.5	8.7	2.5	3.5	29	2.9
CS-3	37.66	0.42	1.57 $\times10^{-5}$	1.46 $\times10^{-4}$	1.5	17	2.5	3.5	34	5.4

469

470

471

View Article Online
DOI: 10.1039/C8CP02703J

Figure captions:

Figure 1: Cross-sectional schematic diagram of PID setup.

Figure 2: Two-diode model DC equivalent circuit.

Figure 3: (a) J-V characteristics of measured CS-1, CS-2 and CS-3 solar cells, with two-diode model fitted curves, (b) Junction resistance with respect to DC bias voltage.

Figure 4: AC equivalent circuits of PID-s affected solar cells (a) CS-1 and (b) CS-2.

Figure 5: FESEM analysis of PID-s affected solar cell with EDX mapping.

Figure 6: Nyquist curves of (a) CS-1 (b) CS-2 and (C) CS-3 solar cells, (d) Comparative frequency-impedance behaviour of three cases.

Figure 7: Effective minority carrier lifetime versus applied voltage bias.

Figure 8: Mott–Schottky response of mc-Si solar cell for CS-1, CS-2 and CS-3**.**

Figure 9: Micro-Raman spectra of initial (CS-1) and PID-s affected solar cell (PID-1, PID-2 and PID-3 represent data obtained from PID-s affected regions as marked by 1, 2 and 3 in the insert).

View Article Online
DOI: 10.1039/C8CP02703J

Figure 1:

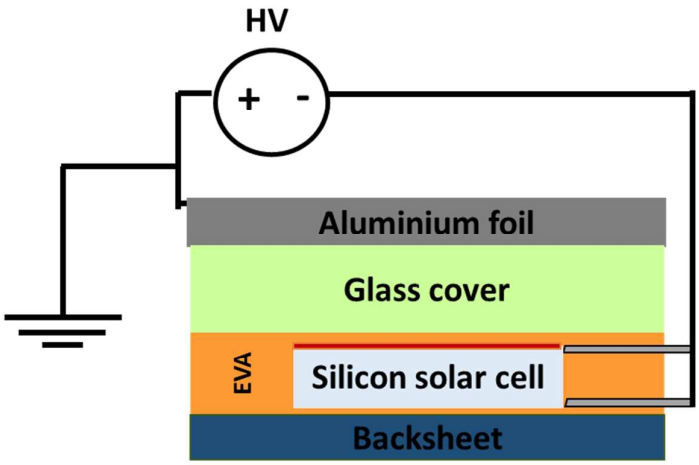

View Article Online
DOI: 10.1039/C8CP02703J

Figure 2:

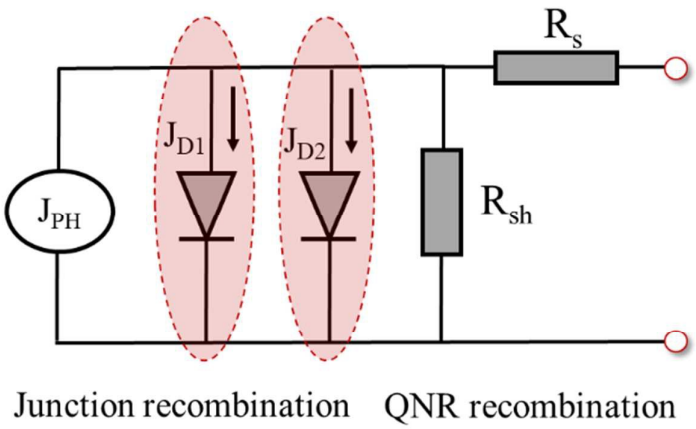

View Article Online
DOI: 10.1039/C8CP02703J

Figure 3:

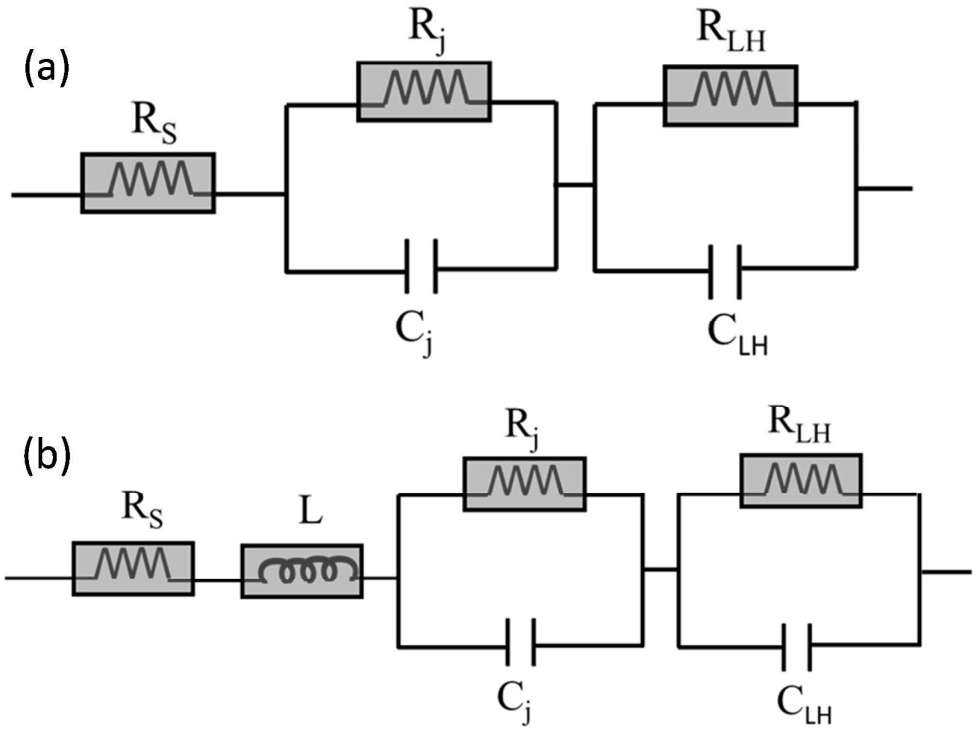

View Article Online
DOI: 10.1039/C8CP02703J

Figure 4:

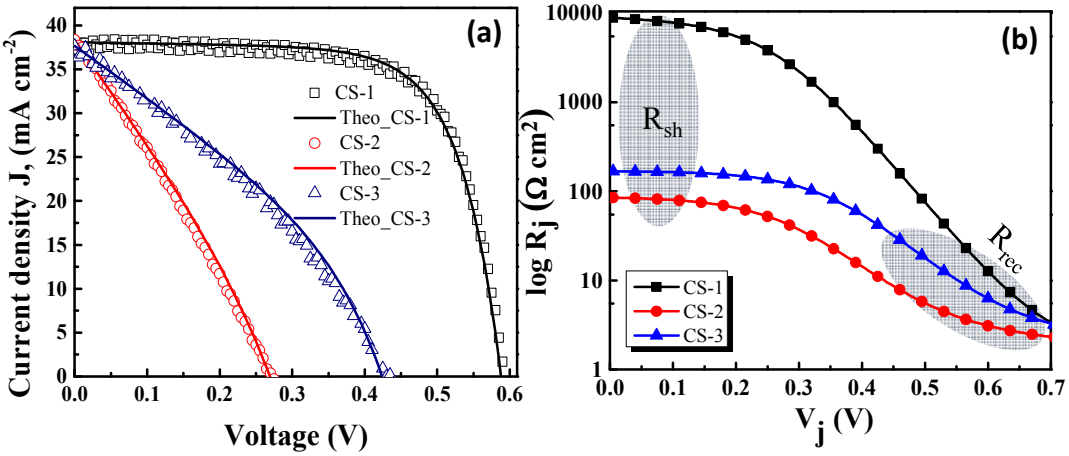

View Article Online
DOI: 10.1039/C8CP02703J

Figure 5:

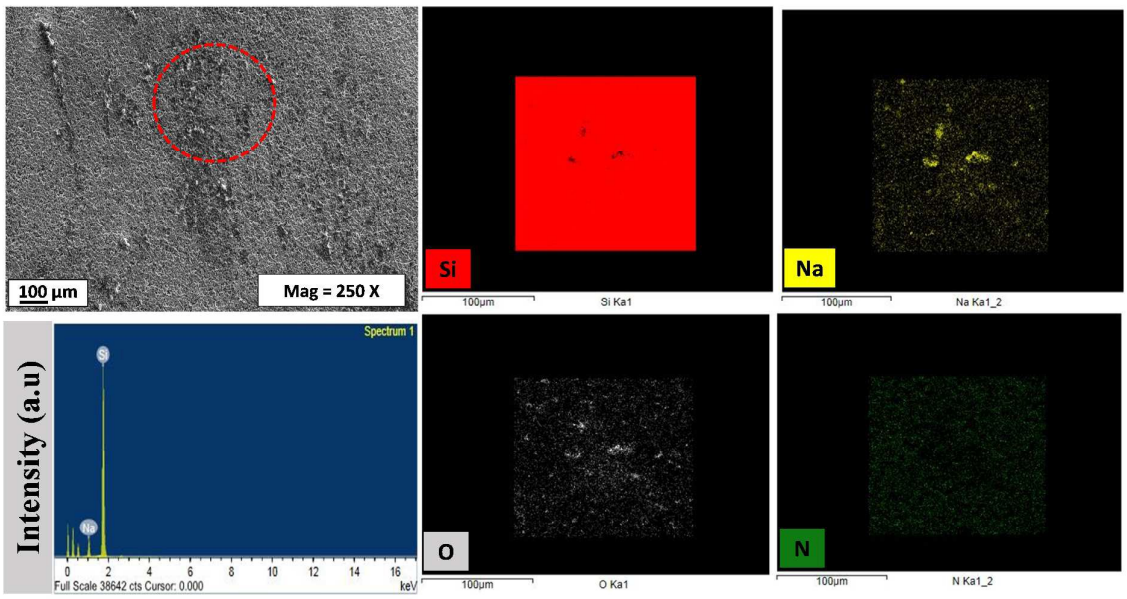

View Article Online
DOI: 10.1039/C8CP02703J

Figure 6:

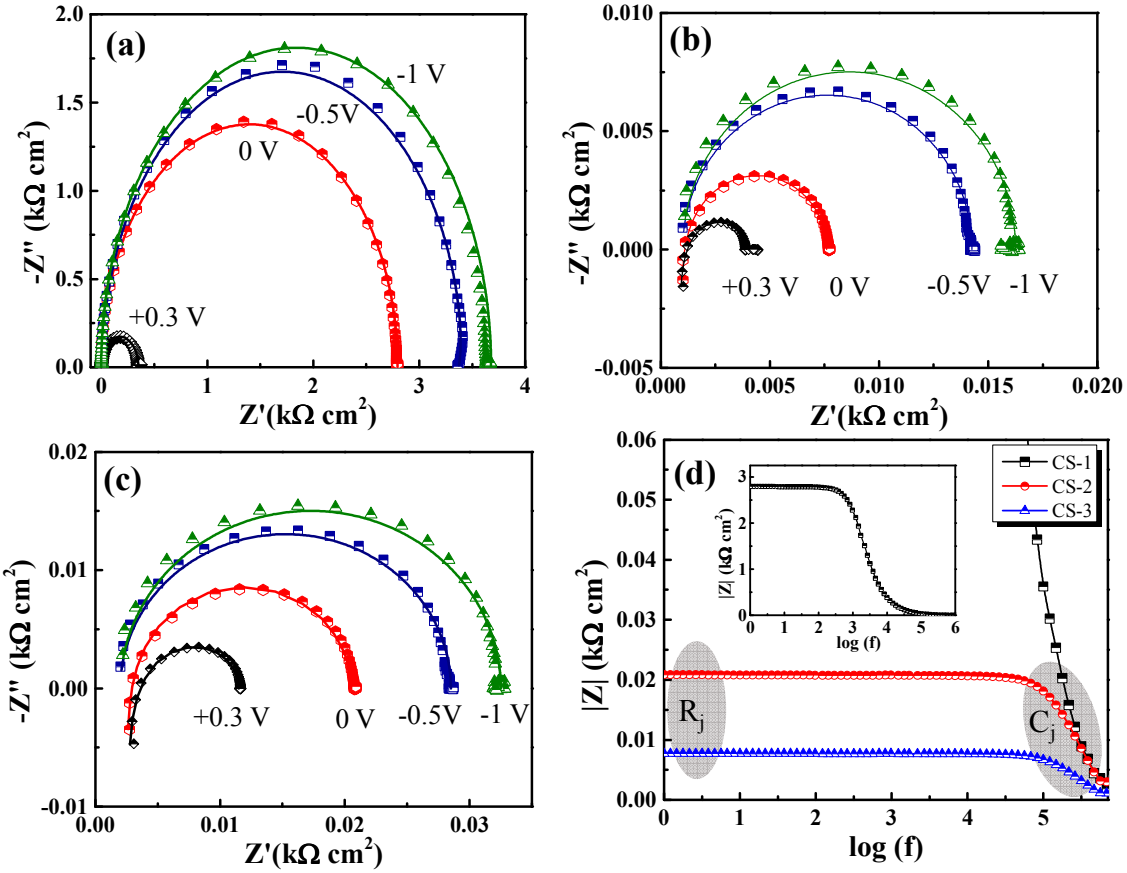

View Article Online
DOI: 10.1039/C8CP02703J

Figure 7:

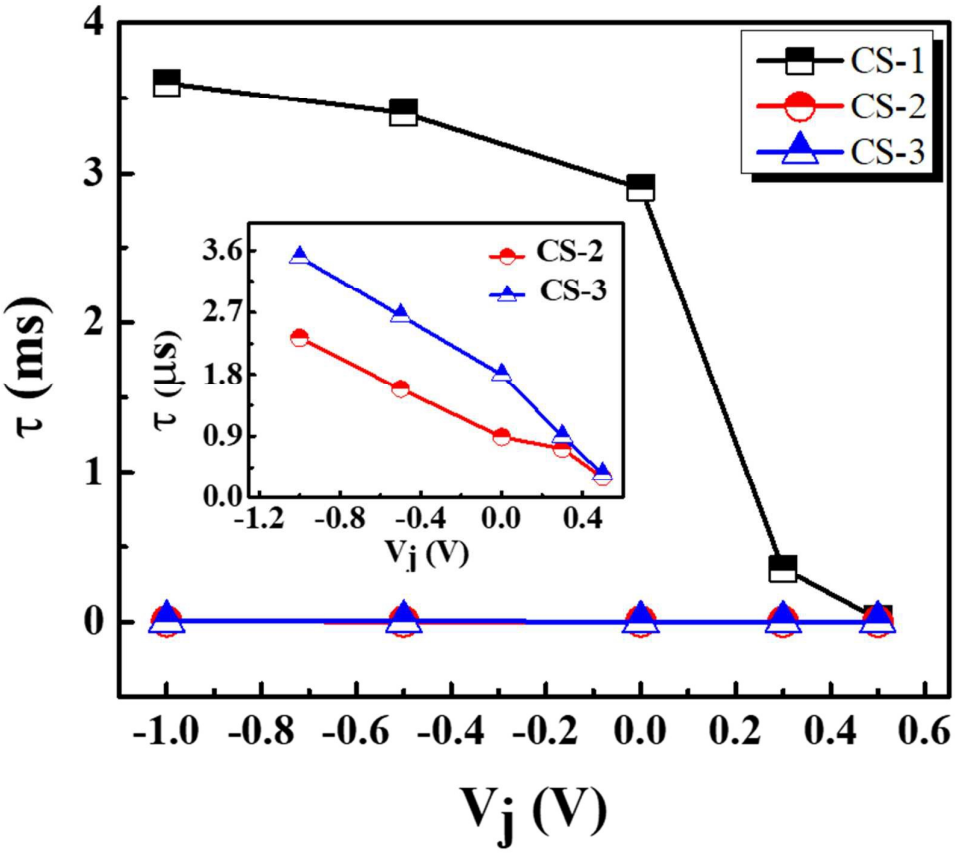

View Article Online
DOI: 10.1039/C8CP02703J

Figure 8:

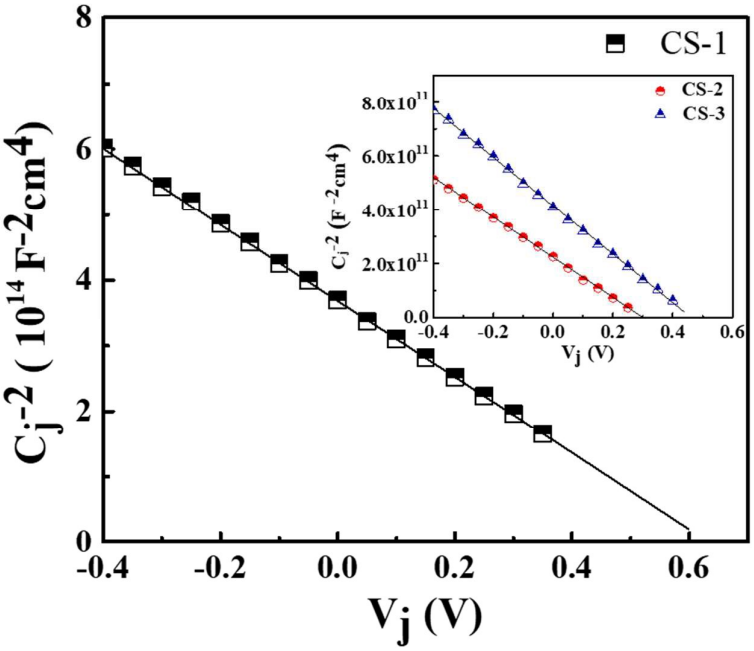

View Article Online
DOI: 10.1039/C8CP02703J

628

629

630 **Figure 9:**

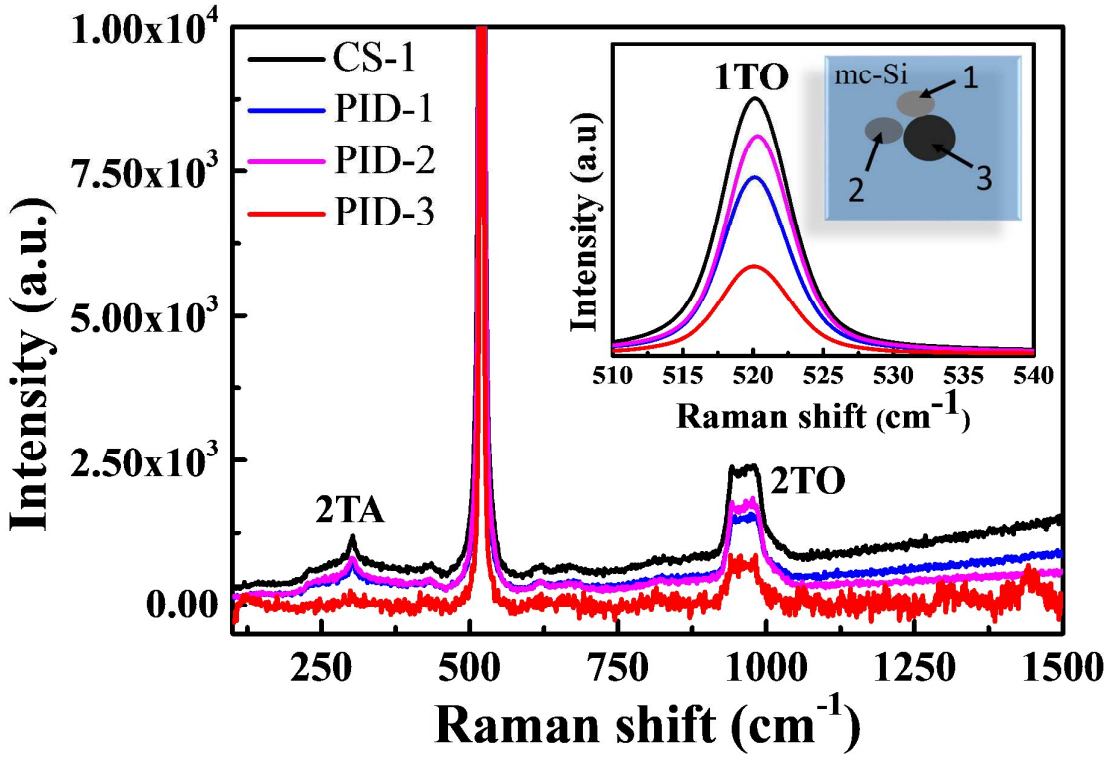

631

632